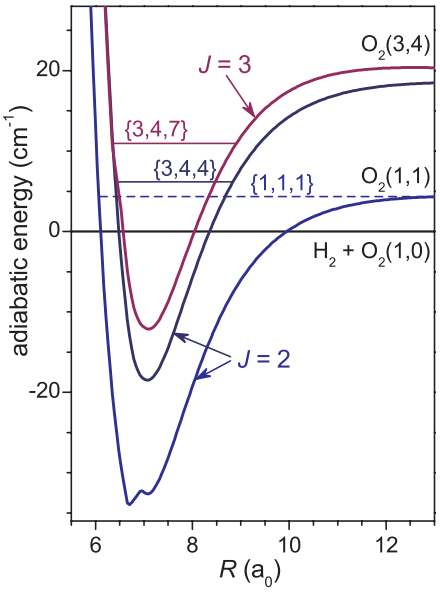

Fig. 3. Adiabatic bender curves with total angular momentum J = 2 and 3 that correlate with O_2 states (N, j) = (1, 1) and (3, 4). Quasi-bound states below (solid lines) or above (dashed lines) the dissociation limit are labeled with their quantum numbers {N,j,l} (see text).

resonance in its rising edge and a Feshbach resonance in its falling edge. The J = 3 curve, which correlates with the O_2 (N = 3, j = 4) + H_2 (j = 0) closed channel, supports a bound state at $E_{3,4,7}$ = 10.94 cm^{-1} in good agreement with the center of peak b. Peak b is thus a pure Feshbach resonance. Analysis of J = 4 is less straightforward, because adiabatic-bender potentials correlating with O_2 (N = 3, j = 2, 3, 4) + H_2 (j = 0) closed channels at $E_{3,2}$ = 16.25 cm^{-1}, $E_{3,3}$ = 18.34 cm^{-1}, and $E_{3,4}$ = 16.39 cm^{-1} are found to support six bound and quasi-bound states situated between 15.3 and 17.1 cm^{-1} (fig. S3). Peak c is a composite of Feshbach resonances.

Our results highlight the purely quantum mechanical nature of this inelastic collision process. None of the partial waves exhibits a long tail, which would indicate nonresonant rotational energy transfer. Successful O_2 (N = 1, j = 0 → N = 1, j = 1) excitation exclusively occurs via shape and Feshbach resonances. Our results also validate the PES, which can now be used with confidence to calculate precise fine-structure resolved low-temperature rate coefficients for rotational (de-)excitation of O_2 ($X^3\Sigma_g^-$) by H_2. This regime is of particular importance for astrophysics because, in the interstellar medium, O_2 rotational level populations result both from radiative transitions and from inelastic collisions with overwhelmingly abundant H_2. Evaluation of O_2 abundance from spectral line data (*24*) requires the accurate knowledge of these rate coefficients.

References and Notes

1. R. D. Levine, R. B. Bernstein, *Molecular Reaction Dynamics and Chemical Reactivity* (Oxford Univ. Press, Oxford, 1987).
2. G. C. Schatz, *Science* **288**, 1599–1600 (2000).
3. A. Schutte, D. Bassi, F. Tommasini, G. Scoles, *Phys. Rev. Lett.* **29**, 979–982 (1972).
4. R. S. Grace, D. L. Johnson, J. G. Skofronick, *J. Chem. Phys.* **67**, 2443 (1977).
5. J. P. Toennies, W. Welz, G. Wolf, *J. Chem. Phys.* **71**, 614 (1979).
6. W. Dong *et al.*, *Science* **327**, 1501–1502 (2010).
7. R. T. Skodje *et al.*, *Phys. Rev. Lett.* **85**, 1206–1209 (2000).
8. A. B. Henson, S. Gersten, Y. Shagam, J. Narevicius, E. Narevicius, *Science* **338**, 234–238 (2012).
9. S. Chefdeville *et al.*, *Phys. Rev. Lett.* **109**, 023201 (2012).
10. M. H. Alexander, P. J. Dagdigian, *J. Chem. Phys.* **79**, 302 (1983).
11. M. Lara *et al.*, *Phys. Rev. Lett.* **109**, 133201 (2012).
12. D. Pentlehner *et al.*, *Rev. Sci. Instrum.* **80**, 043302 (2009).
13. Materials and methods are detailed in the supplementary materials on *Science* Online.
14. S. T. Pratt, P. M. Dehmer, J. L. Dehmer, *Chem. Phys. Lett.* **105**, 28–33 (1984).
15. R. J. Yokelson, R. J. Lipert, W. A. Chupka, *J. Chem. Phys.* **97**, 6153 (1992).
16. Y. Kalugina, O. D. Alpizar, T. Stoecklin, F. Lique, *Phys. Chem. Chem. Phys.* **14**, 16458–16466 (2012).
17. J. M. Hutson, S. Green, MOLSCAT computer code, version 14, 1994, distributed by Collaborative Computational Project No. 6 of the Engineering and Physical Sciences Research Council (UK).
18. F. Lique, M.-L. Senent, A. Spielfiedel, N. Feautrier, *J. Chem. Phys.* **126**, 164312 (2007).
19. F. Lique, *J. Chem. Phys.* **132**, 044311 (2010).
20. M. H. Alexander, S. Gregurick, P. J. Dagdigian, *J. Chem. Phys.* **101**, 2887 (1994).
21. D. T. Colbert, W. H. Miller, *J. Chem. Phys.* **96**, 1982 (1992).
22. D. W. Chandler, *J. Chem. Phys.* **132**, 110901 (2010).
23. H. Feshbach, *Ann. Phys.* **5**, 357–390 (1958).
24. B. Larsson *et al.*, *Astron. Astrophys.* **466**, 999–1003 (2007).

Acknowledgments: This work extends the objectives of ANR-12-BS05-0011-02 contract with the Agence Nationale de la Recherche and contract 2007.1221 with the Conseil Régional d'Aquitaine, for which financial support is gratefully acknowledged. S.C., S.Y.T.v.d.M., C.N., and M.C. acknowledge support of Partenariat Hubert Curien Van Gogh 2013–28484TH contract. S.Y.T.v.d.M. acknowledges support from the Netherlands Organisation for Scientific Research (NWO) via a VIDI grant and from the Université de Bordeaux for a visiting professorship. Y.K. acknowledges the support of High Performance Computing SKIF-Cyberia (Tomsk State University). Y.K. and F.L. acknowledge the financial support of the CNRS national program Physique et Chimie du Milieu Interstellaire and of the Contrat de Projets Etat-Région Haute-Normandie/Centre National de Recherche Technologique/Energie, Electronique, Matériaux.

Supplementary Materials

www.sciencemag.org/cgi/content/full/341/6150/1094/DC1
Materials and Methods
Figs. S1 to S3
Table S1
References (*25*–*33*)

3 June 2013; accepted 18 July 2013
10.1126/science.1241395

Direct Determination of Absolute Molecular Stereochemistry in Gas Phase by Coulomb Explosion Imaging

Martin Pitzer,[1] Maksim Kunitski,[1] Allan S. Johnson,[1,2] Till Jahnke,[1] Hendrik Sann,[1] Felix Sturm,[1] Lothar Ph. H. Schmidt,[1] Horst Schmidt-Böcking,[1] Reinhard Dörner,[1] Jürgen Stohner,[3] Julia Kiedrowski,[4] Michael Reggelin,[4] Sebastian Marquardt,[4] Alexander Schießer,[4] Robert Berger,[4]* Markus S. Schöffler[1]*

Bijvoet's method, which makes use of anomalous x-ray diffraction or dispersion, is the standard means of directly determining the absolute (stereochemical) configuration of molecules, but it requires crystalline samples and often proves challenging in structures exclusively comprising light atoms. Herein, we demonstrate a mass spectrometry approach that directly images the absolute configuration of individual molecules in the gas phase by cold target recoil ion momentum spectroscopy after laser ionization–induced Coulomb explosion. This technique is applied to the prototypical chiral molecule bromochlorofluoromethane and the isotopically chiral methane derivative bromodichloromethane.

A molecule that cannot be superposed with its mirror image by pure translation and rotation is termed chiral, with the non-identical mirror images called enantiomers. If it were not for the predicted tiny contributions due to parity-violating weak interactions (*1*), which are currently searched for in high-precision molecular physics experiments on chiral molecules (*2*, *3*), the energy levels of both enantiomers would be equal. The enantiomers can be distinguished by their interaction with other chiral objects; for instance, left- or right-handed molecules and left- or right-handed circularly polarized photons. The interaction with polarized light led Louis Pasteur, more than one and a half centuries ago, to the discovery of molecular chirality by observing optical rotation in aqueous solutions of manually separated enantiomorphic crystals from double salts of tartaric acid (*4*). van't Hoff (*5*) and Le Bel (*6*) independently ascribed Pasteur's

[1]Institute for Nuclear Physics, Johann Wolfgang Goethe-Universität Frankfurt, Max-von-Laue-Straße 1, 60438 Frankfurt, Germany. [2]University of Ottawa, Ottawa, ON K1N 6N5, Canada. [3]Institute of Chemistry and Biological Chemistry, Zurich University of Applied Sciences, Campus Reidbach, Einsiedlerstrasse 31, 8820 Wädenswil, Switzerland. [4]Clemens-Schöpf Institute, Technische Universität Darmstadt, Petersenstraße 22, 64287 Darmstadt, Germany.

*Corresponding author. E-mail: schoeffler@atom.uni-frankfurt.de (M.S.S.); robert.berger@tu-darmstadt.de (R.B.)

observation to an underlying three-dimensional (3D) structure of molecules, which can result in two nonidentical mirror image structures.

Enantiomers can be distinguished comparatively easily by their chiroptical signals, such as optical rotation, that are of (nearly, due to parity violation) equal magnitude but opposite sign. This is manifested by the frequently used phenomenological (+/−) terminology. The microscopic structure, on the other hand, is classified with the systematic *R*/*S* or *P*/*M* stereodescriptors (*7*). However, assigning the absolute (stereochemical) configuration—that is, establishing which of the two possible mirror image spatial structural models gives rise to optical rotation with positive or negative sign—still poses a challenge.

The standard approach to directly determining absolute configuration is Bijvoet's method (*8*) of 1951, but in 2001 the technique of Coulomb explosion imaging (CEI) (*9*) was shown to be a potential means to determine the handedness of chiral molecules (*10*). Before 1951, chemical or biochemical conversions were used that relate compounds of unknown configuration to others with known configuration, a method that is still applied today. For this purpose, Fischer (*11*) had arbitrarily assigned a given 3D structural model (denoted as the D form) of saccharic acid to the compound that is weakly (+) rotating in aqueous solution and its mirror image (L form) to the (−) rotating counterpart. Subsequently [see also (*12*) for the historical development], catalogs of the D and L series were established, the components of which were chemically related, either directly to D- or L-saccharic acid or to other chiral molecules already filed in the catalog. Bijvoet finally confirmed (*8*) Fischer's arbitrary choice by studying the sodium rubidium double salt of tartaric acid with anomalous x-ray diffraction. Heavy elemental scatterers induce a pronounced phase and intensity shift when irradiated with x-rays near their absorption edge, which allows the determination of absolute configuration. Although typically quite conclusive, Bijvoet's method is limited by requiring crystalline samples. A promising new approach using x-ray diffraction has recently been presented by Inokuma *et al.* (*13*). They diffused a dissolved chiral compound into a crystalline host framework containing heavy atoms. As a result of the interaction, the framework's symmetry changed to a chiral space group, thus allowing the application of anomalous x-ray diffraction. Nonetheless, conventional crystallographic challenges and flaws—such as misassigned atoms, symmetry problems, and guest disorder—persist and, hence, require support from mass spectrometry or nuclear magnetic resonance (NMR) (*13*).

The lack of versatile direct approaches has led to the active exploration of indirect physicochemical approaches based on optical rotation and circular dichroism. Indirect methods rely on quantum chemical calculations or empirical rules to interpret the experimental data. Alternatively, liquid chromatography with an enantioselective stationary phase is a widespread method for chiral discrimination. Its drawback for assignment lies in the need for a suitable analog with known stereochemical configuration. Recent activities focus on NMR spectroscopy, either by seeking to turn NMR directly into a chiroptical method (*14*) or by exploring possibilities to use residual dipolar couplings in chiral nonracemic alignment media (*15*). Also, photoelectron circular dichroism has received renewed interest (*16*), and promising three-wave mixing strategies to obtain chiroptical signals in microwave spectroscopy have been reported recently (*17*).

Herein, we focus on direct determination of absolute configuration in the gas phase by a molecular imaging technique that displays the 3D structure of individual chiral molecules on a detector and thereby permits assignment of absolute configuration on a single-molecule basis. As an alternative to displaying the full structure, one can also 3D-align the molecule and image decisive fragments (*18*). Kitamura *et al.* used a similar approach to ours, but with highly charged argon atoms from an ion source as ionizing agents, to detect dynamical chirality in perdeuterated

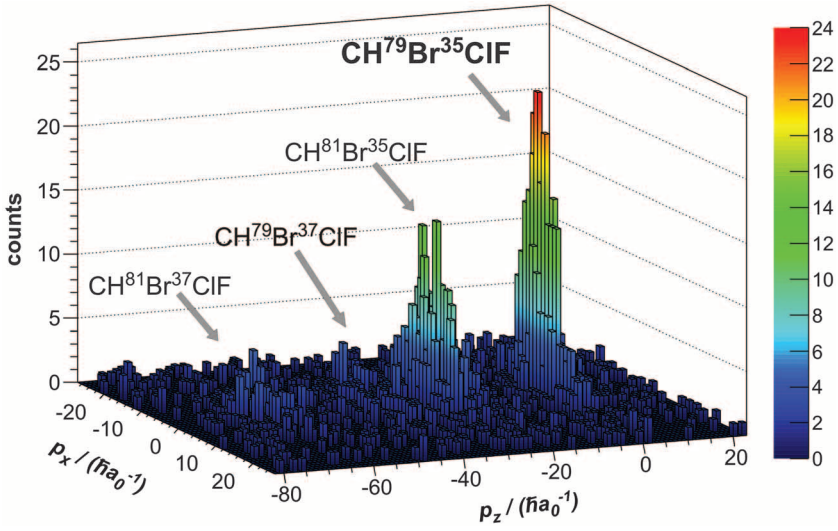

Fig. 1. Sum of linear momentum (*p*) components in fivefold ionization of CHBrClF, demonstrating the excellent resolution achieved in this experiment. Those events detected with p_x and p_z close to zero correspond to a fragment assignment to $^{79}Br^+$, $^{35}Cl^+$, $^{19}F^+$, $^{12}C^+$, and $^1H^+$ (denoted in bold). Fragments of other isotopologues can also be identified but are not used in the present analysis. The atomic unit for momentum is defined as $\hbar a_0^{-1} \approx 1.992 \cdot 10^{-24}$ kg m s^{-1} ($\hbar$, Planck's constant h divided by 2π; a_0, Bohr radius).

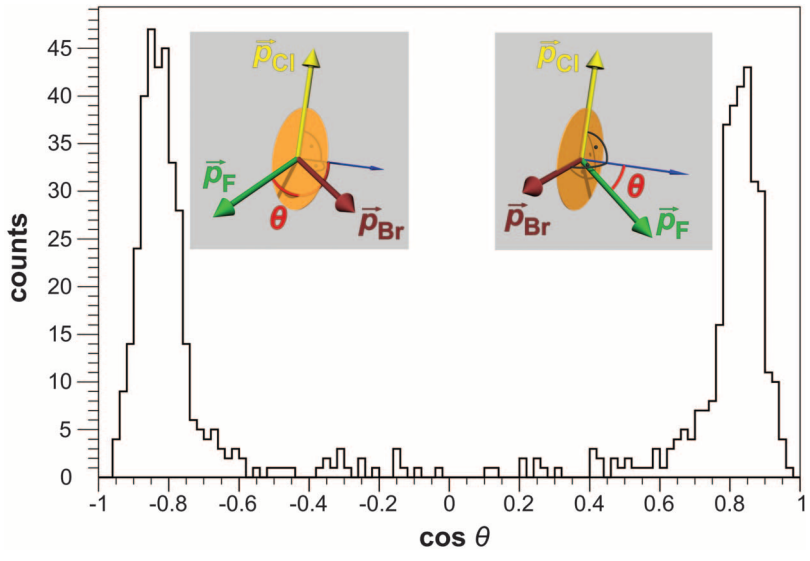

Fig. 2. Chiral discrimination for CHBrClF. The histogram for the cosine of the chirality angle θ shows the clear separation between enantiomers in our racemic sample of CHBrClF. As is illustrated in the insets, the angle is defined via $\cos(\theta) = \vec{p}_F \cdot (\vec{p}_{Cl} \times \vec{p}_{Br})(|\vec{p}_F||\vec{p}_{Cl} \times \vec{p}_{Br}|)^{-1}$. The peak at negative values of cos(θ) corresponds to the *S* enantiomer, whereas the one at positive values corresponds to the *R* enantiomer.

methane (*10*) and pointed out the possibility of detecting molecular handedness. In 2008, Gagnon *et al.* employed a related variant to study the structure of achiral dichloromethane (CH_2Cl_2) (*19*) by CEI. For the direct assignment of the absolute configuration, high count rates for fourfold or higher fragmentation coincidence events are required. The laser systems commercially available in 2008 were unable to produce such rates. To overcome these technical limitations for stereochemical assignments, we combine the latest high-power femtosecond lasers [with repetition rates that are 10 to 100 times higher (100 kHz)] with improved fast hexanode delay-line detectors to surmount otherwise prohibitively long data acquisition time. In addition, we employ high-performance data recording techniques, together with an offline analysis protocol, to cope with the increasing complexity emerging for polyatomic molecules (*20*). These improvements enable the use of CEI to determine the absolute configuration of the prototypical chiral compound bromochlorofluoromethane (CHBrClF) and isotopically chiral methane derivatives in natural abundance such as $CHBr^{37}Cl^{35}Cl$.

$CHBrCl_2$ is commercially available and was used without further purification, as impurities

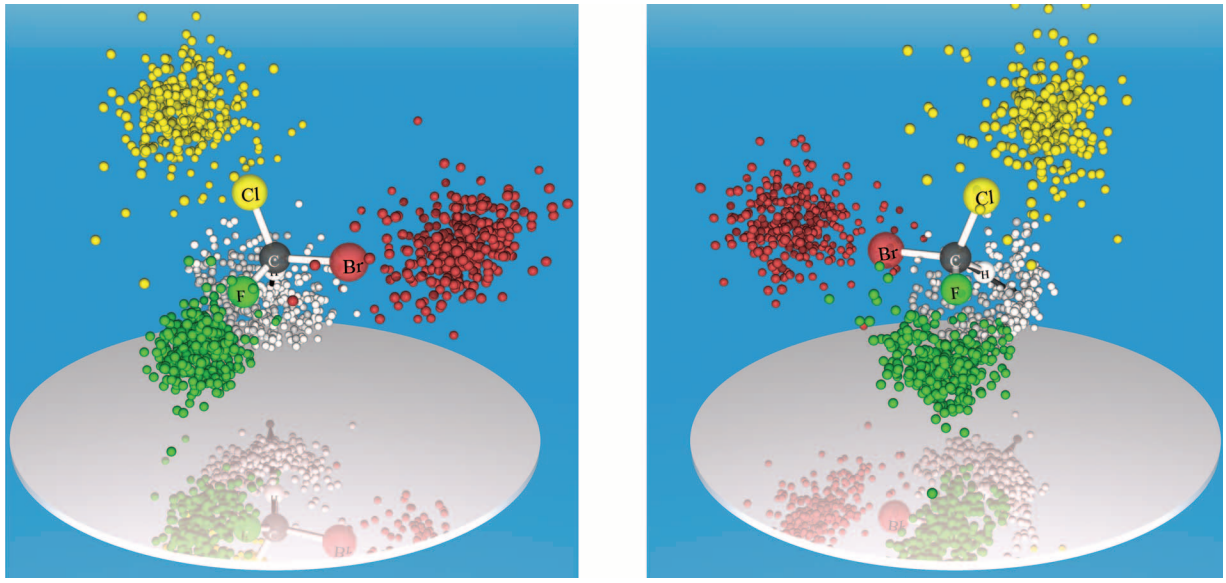

Fig. 3. Linear momenta in fivefold fragmentation of CHBrClF enantiomers. Measured linear momenta in the fivefold fragmentation of (**left**) (*S*)-CHBrClF [$\cos(\theta) < -0.6$] and (**right**) (*R*)-CHBrClF [$\cos(\theta) > 0.6$] are indicated by the following color codes: C, gray arrow; H, white; F, green; Cl, yellow; Br, red. Momenta are rotated to the molecular frame of reference, defined by the momentum of the carbon ion and the momentum sum of the bromine and chlorine ions. All momenta are normalized with respect to the carbon momentum. For better visibility, hydrogen momenta are expanded by a factor of 2. Whereas the substituents are expelled during the Coulomb explosion into the directions expected from the classical structural model, the central atom C is also accelerated away from the center of mass and ejected in a similar direction as hydrogen. An animated version of the figure can be found in the supplementary materials (movies S1 and S2).

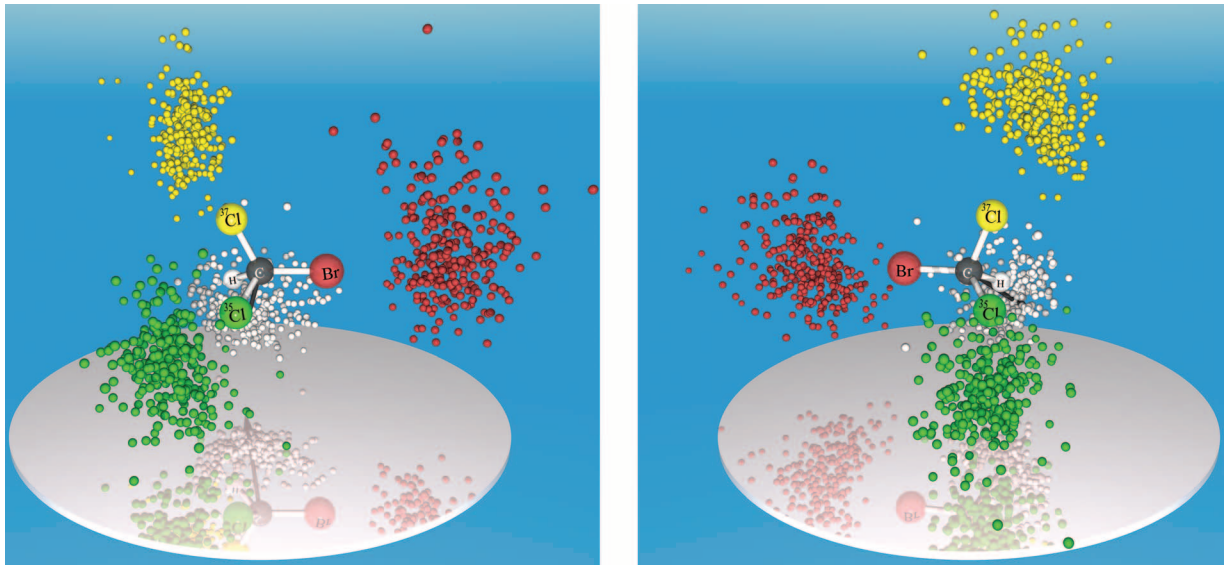

Fig. 4. Measured linear momenta in the fivefold fragmentation of (*S*)-$CH^{79}Br^{37}Cl^{35}Cl$ (left) and (*R*)-$CH^{79}Br^{37}Cl^{35}Cl$ (right). The color codes used correspond to: C, gray arrow; H, white; ^{35}Cl, green; ^{37}Cl, yellow; Br, red. Momenta are rotated to the molecular frame of reference, defined by the momentum of the carbon ion and the momentum sum of ^{79}Br and ^{35}Cl, and normalized with respect to the momentum of the carbon ion. Again, the hydrogen momentum is scaled by a factor of 2. A histogram and an animated version of the figure can be found in the supplementary materials (fig. S5 and movies S3 and S4). For a wider angle of vision, see fig. S7, where a few outlier signals also become clearly visible.

are easily discarded in the analysis step of coincidence experiments. Racemic CHBrClF was synthesized as described in (*21*) by reacting $CHBr_2Cl$ with HgF_2. The spectrometer system employed was described in detail in (*22*). For the present study, the setup was augmented by an assembly of cold traps to recycle the volatile sample compounds.

The approach for direct determination of absolute configuration employs the well-established cold target recoil ion momentum spectroscopy (COLTRIMS), as depicted in fig. S1 in the supplementary materials. A supersonic gas jet of chiral molecules (*y* axis in the laboratory system) crosses a high-power femtosecond laser (laboratory *x* axis) to induce multiple ionization and the resulting Coulomb explosion. Charged fragments are projected by a static electric field along the laboratory *z* axis onto a position- and time-sensitive multichannel plate detector (MCP) with hexagonal delay-line readout (*23*), where all fragments are detected in coincidence (fig. S2). From the impact position on the detector (*x*, *y*) and the known distance between the ionization zone and MCP, as well as the measured time-of-flight, the velocities of all cations (formed in coincidence) can be derived. By assigning masses and charges to the various fragments, corresponding linear momenta of all detected particles can be obtained. In molecular multiple ionization and fragmentation, the momenta of photons and electrons are usually negligible compared with the momenta of the Coulomb exploding ionic fragments. Hence, in a cold molecular beam, the sum of the ion momentum vectors must be close to zero because of momentum conservation. The mass assignment can, therefore, be confirmed by checking this computed total momentum of all ions. Assignment of absolute configuration is, in principle, already possible, once four charged fragments (e.g., Br^+, Cl^+, F^+, and CH^+ for CHBrClF) are detected in coincidence. Signatures of those breakups could be found in the data and used for assignment (results not reported here). Herein, however, we focus on the complete fragmentation into five singly charged ions, because analysis and interpretation are more straightforward. Additionally, the background can be suppressed quite efficiently. Mass resolution in COLTRIMS is sufficient to distinguish various isotopes of bromine and chlorine in natural abundance, thereby even allowing stereochemical characterization of isotopically chiral molecules. Further details of the measurement method can be found in the supplementary materials (*24*).

Figure 1 shows the sum of all ion momenta in the case where five fragments of CHBrClF are measured in coincidence. The peak at zero total momentum shows events with the correct mass assignment: $^{79}Br^+$, $^{35}Cl^+$, $^{19}F^+$, $^{12}C^+$, and $^{1}H^+$. These events were used for the determination of the absolute configuration. The peaks at lower momentum in the *z* direction are contributions from other isotopologues.

Figure 2 demonstrates the capability to distinguish enantiomers in our racemic sample. For this purpose, an angle θ is defined, indicating if the momenta of bromine, chlorine, and fluorine form a right- or left-handed coordinate system. As distinct peaks are obtained in the histogram, almost all events can be assigned clearly to one enantiomer or the other. This shows the robustness of our method against the laser pulse length: Being ~40-fs long, our pulses are not short enough to consider the hydrogen frozen during multiple ionization. The clear separation of enantiomers in the histogram indicates, however, that the motion of hydrogen during the laser pulse does not alter bond angles to an extent that would prevent identification of enantiomers. These results also show that reconstruction of the exact geometric structure is not necessary for the determination of absolute configuration. Classical molecular dynamics simulations confirm that the enantiomers are mapped unambiguously onto their momentum space analogs that are presented here.

Figure 3 overlays measured linear momenta on a rigid structural model of neutral CHBrClF, with the linear momentum of carbon fixed along the *x* axis, the momentum sum of chlorine and bromine defining the *xy* plane, and all other linear momenta being oriented relative to these. For better visibility, momenta are normalized with respect to the carbon momentum. The momentum of hydrogen, being very small due to the low mass, is expanded by a factor of 2 in this figure. It is evident that the configuration of the two enantiomers is directly imaged on the detector. As a racemic mixture of CHBrClF was employed, an equal ratio for the *S* and *R* configurations was obtained within the statistical uncertainty [329 and 302 events for *S* and *R*, respectively, with $|\cos(\theta)| > 0.6$ in each case]. At first sight, one might be surprised that the carbon ion is detected in the same direction as the proton. This is due to the fact that the position of the center of mass is conserved; thus, H^+ and C^+, as the lightest two ions of the system, are repelled from the slowly moving heavier ions, as has been confirmed with the help of molecular dynamics simulations.

For CHBrClF, the direct assignment of absolute configuration works unequivocally in the majority of fivefold coincidence events because of the comparatively large mass difference between the ions. The situation is considerably more challenging for the case of isotopically chiral systems. In the case of $CHBrCl_2$ (Fig. 4), not all fivefold fragmentation events allow an unambiguous assignment of the isotope masses to each fragment; hence, no determination of absolute configuration is possible for such events. However, a subset of events that permit a conclusive assignment can be selected by a procedure detailed in the supplementary materials (figs. S3 and S4 and supplementary text). Again, as a racemic sample was used, an almost 50:50 ratio of *S*:*R* is detected [282:273 events (not corrected for outliers) with $|\cos(\theta)| > 0.6$] (see fig. S5).

The technique still has several limitations: Volatile molecules and a large amount of substance are required due to the molecular beam source. Comparatively simple, rigid structures were studied. In the case of more complicated molecules, the kinematic properties of the fragments may not directly illustrate the geometric structure, making the identification of the absolute configuration less straightforward. In this case, geometrical reconstruction or comparison with simple molecular dynamics simulations might become necessary, especially when several stereogenic elements are present. On a technical level, the probability of multifragment detection decreases dramatically with the increasing amount of fragments, as both the fragmentation yield and the detection efficiency diminish exponentially with the increasing number of fragments.

Stepwise fragmentation is a limitation as well. Additionally, when multiple ionization is slow compared with vibrational time scales, assignment can be hampered or even completely prohibited. For this purpose, faster ionization schemes with shorter laser pulses and higher laser intensity are required.

The present imaging approach allows for determination of absolute configuration of gas phase molecules on a per-molecule basis. Apart from a rigid structural model, it does not require theoretical input. Besides structure determination, as demonstrated herein, the coincidence technique creates opportunities to study chirality in single molecules.

References and Notes

1. R. Berger, in *Relativistic Electronic Structure Theory, Part 2: Applications*, P. Schwerdtfeger, Ed. (Elsevier, Netherlands, 2004), pp. 188–288.
2. C. Daussy *et al.*, *Phys. Rev. Lett.* **83**, 1554–1557 (1999).
3. M. Quack, J. Stohner, M. Willeke, *Annu. Rev. Phys. Chem.* **59**, 741–769 (2008).
4. L. Pasteur, in *Leçons de Chimie Professées en 1860 par MM. Pasteur, Cahours, Wurtz, Berthelot, Sainte-Claire Devile, Barral et Dumas* (Hachette, Paris, 1861), pp. 1–48.
5. J. H. van't Hoff, *Arch. Néerl. Sci. Exactes Nat.* (French transl.) **9**, 445–454 (1874).
6. J.-A. Le Bel, *Bull. Soc. Chir. Paris* **T22**, 337–347 (1874).
7. R. S. Cahn, C. Ingold, V. Prelog, *Angew. Chem. Int. Ed. Engl.* **5**, 385–415 (1966).
8. J. M. Bijvoet, A. F. Peerdeman, A. J. van Bommel, *Nature* **168**, 271–272 (1951).
9. Z. Vager, R. Naaman, E. P. Kanter, *Science* **244**, 426–431 (1989).
10. T. Kitamura, T. Nishide, H. Shiromaru, Y. Achiba, N. Kobayashi, *J. Chem. Phys.* **115**, 5 (2001).
11. E. Fischer, *Ber. Dtsch. Chem. Ges.* **24**, 2683–2687 (1891).
12. F. W. Lichtenthaler, *Angew. Chem. Int. Ed. Engl.* **31**, 1541–1556 (1992).
13. Y. Inokuma *et al.*, *Nature* **495**, 461–466 (2013).
14. A. D. Buckingham, *Chem. Phys. Lett.* **398**, 1–5 (2004).
15. R. Berger *et al.*, *Angew. Chem. Int. Ed.* **51**, 8388–8391 (2012).
16. C. Lux *et al.*, *Angew. Chem. Int. Ed.* **51**, 5001–5005 (2012).
17. D. Patterson, J. M. Doyle, *Phys. Rev. Lett.* **111**, 023008 (2013).
18. J. L. Hansen *et al.*, *J. Chem. Phys.* **136**, 204310 (2012).
19. J. Gagnon, K. F. Lee, D. M. Rayner, P. B. Corkum, V. R. Bhardwaj, *J. Phys. B* **41**, 215104 (2008).

20. B. Wales *et al.*, *Nucl. Instrum. Methods Phys. Res. A* **667**, 11–15 (2012).
21. J. Hine, A. M. Dowell, J. E. Singley, *J. Am. Chem. Soc.* **78**, 479–482 (1956).
22. J. Ullrich *et al.*, *Rep. Prog. Phys.* **66**, 1463–1545 (2003).
23. O. Jagutzki *et al.*, *IEEE Trans. Nucl. Sci.* **49**, 2477–2483 (2002).
24. Further details on the measurement principle, with six additional figures and four movies, are available in the supplementary materials on *Science* Online.

Acknowledgments: This paper is dedicated to Helmut Schwarz on the occasion of his 70th birthday. We thank D. Avnir, T. Isaev, and F. Lichtenthaler for discussion; M. Meckel for help with some figures; and A. Czasch for support concerning data analysis. This work was supported by the State Initiative for the Development of Scientific and Economic Excellence (LOEWE) in the LOEWE-Focus ELCH. The momentum data used to draw the figures are provided in the supplementary materials. Raw data are archived at the University of Frankfurt and are available upon request.

Supplementary Materials
www.sciencemag.org/cgi/content/full/341/6150/1096/DC1
Supplementary Text
Figs. S1 to S7
Reference (*25*)
Movies S1 to S5
Databases S1 and S2

10 May 2013; accepted 2 August 2013
10.1126/science.1240362

Achieving the Convention on Biological Diversity's Goals for Plant Conservation

L. N. Joppa,[1]* P. Visconti,[1] C. N. Jenkins,[2] S. L. Pimm[3]*

Identifying which areas capture how many species is the first question in conservation planning. The Convention on Biological Diversity (CBD) aspires to formal protection of at least 17% of the terrestrial world and, through the Global Strategy for Plant Conservation, 60% of plant species. Are these targets of protecting area and species compatible? We show that 67% of plant species live entirely within regions that comprise 17% of the land surface. Moreover, these regions include most terrestrial vertebrates with small geographical ranges. However, the connections between the CBD targets of protecting area and species are complex. Achieving both targets will be difficult because regions with the most plant species have only slightly more land protected than do those with fewer.

Protected areas are broadly effective (*1*–*6*) and thus usually necessary, if not always sufficient, to protect species. Their effective allocation is vital to slow present extinction rates that are 100 to 1000 times faster than the natural background rate (*7*). The Convention on Biological Diversity's (CBD's) 20 Aichi Targets—agreed in October 2010 in Nagoya, Japan—extend to 2020 an international commitment to halt biodiversity loss (www.cbd.int/sp/targets/). Target 11 seeks formal protection of >17% of the terrestrial world. One can use the most taxonomically complete and spatially best-resolved data on species distributions (*8*)—birds (*9*), mammals (*10*), and amphibians (*10*)—to assess this target (*11*). Unfortunately, these are a taxonomically limited subset of ~23,000 terrestrial species from more than a million described animal species with many more as-yet unknown (*12*). This raises concerns about their representativeness for setting global conservation priorities. By contrast, plants form a large taxonomic sample with >350,000 described species and ~15% awaiting description (*13*). Important in themselves, plants influence the diversity of insects (*14*) and other animals. In 2010, the CBD updated the Global Strategy for Plant Conservation (GSPC) (*11*), seeking protection for 60% of plant species as a critical indicator toward CBD goals. Are these targets of protecting area and species compatible?

Satisfying the joint aspirations of the CBD's Aichi Target 11 and the GSPC will be difficult. First, by 2009, the world had protected ~13% of global land area (*15*), but half of the world's major habitat divisions—ecoregions (*16*)—did not meet a target of 10% coverage. Some ~75% of them had <10% of their area strictly protected (*15*). Present conservation efforts bias toward lands that are high, cold, dry, or otherwise far from people—often a mismatch with where conservation needs are pressing (*17*). These statistics show that protected areas are not representative of terrestrial environments, but they do not address species targets directly.

Second, for plants, as for most taxa, unresolved issues of taxonomy generate uncertainties in how many species there are amid existing catalogs of described species and how many are still missing from them (*13*, *18*). Target 1 of the GSPC is to complete "a widely accessible working list of all known plant species, as a step toward a complete world flora" (*19*). Major international botanic gardens responded in 2010 with "The Plant List" (www.theplantlist.org)—a working list of all known plant species. Here, we analyze a subset of ~109,000 species taken from the World Checklist of Selected Plant Families (WCSP) (*20*). For this subset, literature compilers and taxonomists have attempted a consensus overview of the current state of knowledge of select families, including correct names for currently accepted species and their synonyms. For this quarter of the world's plant species, we previously predicted where as-yet undescribed species likely live (*18*).

Third, species' distributional data are imperfect (*21*). Elsewhere, we map birds, mammals, and amphibians on a scale of 10 km by 10 km (*8*). We compare them to plant distributions below. The details of these animal distributions are exceptional; plant distributional data are coarser. Flowering plant species in the WCSP are tagged to one or more of the 369 countries or geographic regions delineated by the International Taxonomic Database Working Group (*22*). Further details on the species and regions are in the supplementary materials (*23*). Nonetheless, this spatial scale captures the essential first step of comparing targets of area protected to species protected.

More problematic is that plant distributional data are species lists from regions where the largest region is 2 million times the area of the smallest. For the biodiversity hotspots of Myers *et al.* (*24*), the ratio is ~130. The relationships of numbers of species (S) to area (A) are well described by $S = cA^z$; c and z are parameters. Because z is <1, species densities, S/A, generally decline with increasing area. This makes objective comparisons of areas—and the designation of conservation priorities—challenging. On the basis of species' totals alone, apparent priorities tend to be the largest regions; those based on species' densities, the smallest ones. Further complicating matters, z depends on circumstance: Islands, continuous areas within continents, and biogeographically unrelated regions have different characteristic values (*25*). This fact dashes hopes of a single, global correction of species' numbers by a simple function of area to permit regional comparisons.

We can address this issue directly, because our results fall from quantitative databases and not the expert opinions used by Myers *et al.*, which are impossible to replicate or update. Our solution uses a greedy algorithm to accumulate species found only within a progressively larger set of regions ("endemic densities"; Fig. 1 and table S1b). We scale our results to 100,000 plant species and to 1000 km^2.

Regions with the highest densities enter first, followed by those adding progressively fewer new species to the aggregated total. Thus, the first 43 regions to enter are all islands, followed by Costa Rica. In the data that we consider, Costa Rica has 791 endemics and adds all of these, reducing the accumulated endemic density to 29. Panama enters next. It has 775 endemics, but adds

[1]Microsoft Research, 21 Station Road, Cambridge CB1 2FB, UK. [2]Department of Biological Sciences, North Carolina State University, Box 7617, Raleigh, NC 27606, USA. [3]Nicholas School of the Environment, Duke University, Box 90328, Durham, NC 27708, USA.

*Corresponding author. E-mail: stuartpimm@me.com

Editor's Summary

Absolute Images

Molecules are held together by a balance of charge between negative electrons and positive nuclei. When multiple electrons are expelled by laser irradiation, the remaining, mutually repulsive nuclei fly apart in a Coulomb explosion. Instead of traditional x-ray diffraction methods that require crystalline samples, **Pitzer *et al.*** (p. 1096) show that by tracking the fragment trajectories from laser-induced Coulomb explosions of relatively simple gas phase molecules, they can determine the absolute stereochemical configuration of enantiomers (mirror-image isomers).